THESIS FOR THE DEGREE OF LICENCIATE OF ENGINEERING

Everything is imperfect: Studies on point defects in insulators

CHRISTOPHER LINDERÄLV

Department of Physics
CHALMERS UNIVERSITY OF TECHNOLOGY
Göteborg, Sweden 2020

Everything is imperfect:
Studies on point defects in insulators
CHRISTOPHER LINDERÄLV

© Christopher Linderälv, 2020

Department of Physics
Chalmers University of Technology
SE-412 96 Göteborg, Sweden
Telephone +46 31 772 10 00

Chalmers reproservice
Göteborg, Sweden 2020

Everything is imperfect:
Studies on point defects in insulators

Christopher Linderälv
Department of Physics
Chalmers University of Technology

Abstract

Point defects can be detrimental or absolutely necessary for the performance of a material. Due to the implications defects have on a material, defects have been widely studied over the last century. However, there are plenty of open questions that concerns the effect of point defects in materials but also properties of defects that are common across materials. This thesis consists of studies on equilibrium properties of oxygen vacancies and optical lineshapes of transitions on point defects.

Using first principles calculations, general properties of oxygen vacancies in wide band gap oxides are revealed. The induced defect level of the oxygen vacancy is found to be constant in a number of materials. It is often located in the middle of the band gap and associated with a large structural distortion upon a change in charge state. Due to the large structural distortion, oxygen vacancies may play a role in luminescence quenching in oxide based phosphors and recombination processes in general. A possible recombination mechanism involving oxygen vacancies is proposed in the oxide phosphor Ce:YAG, which could explain the luminescence quenching.

In connection with luminescence quenching in Ce:YAG, the origin of the phonon side bands of the optical transition is elucidated. Due to the connection between the optical lineshape and the geometry of a point defect, the optical lineshape can be used to identify point defects. The point defect emission in hexagonal boron nitride is addressed and several point defects can be matched to observed emission lines.

Keywords: wide band gap oxides, point defects, optical lineshape, oxygen vacancies, band alignment, density functional theory, boron nitride, insulator

LIST OF PUBLICATIONS

This thesis consists of an introductory text and the following publications:

I **A Unifying Perspective on Oxygen Vacancies in Wide Band Gap Oxides**
Christopher Linderälv, Anders Lindman and Paul Erhart
The Journal of Physical Chemistry Letters, **9**, 222-228 (2018)

II **Luminescence quenching via deep defect states: A recombination pathway via oxygen vacancies in Ce-doped YAG**
Christopher Linderälv, Daniel Åberg and Paul Erhart
In manuscript

III **A library of vibrational signatures for the identification of single-photon emitters in hexagonal boron nitride**
Christopher Linderälv, Witlef Wieczorek, Paul Erhart
In manuscript

Specification of my contribution to the publications:

I The author performed parts of the calculations, analysis and preparation of figures. The author prepared a first draft of the paper.

II The author performed the calculations pertaining to defects and prepared all figures and a first draft of the paper.

III The author performed all calculations and wrote the paper.

THE FOLLOWING PUBLICATIONS ARE NOT INCLUDED IN THIS THESIS

Interlayer exciton dynamics in van der Waals heterostructures
Simon Ovessen, Samuel Brem, Christopher Linderälv, Mikael Kuisma, Tobias Korn, Paul Erhart, Malte Selig and Ermin Malic
Communications Physics **2**, 23 (2019)

Impact of strain on the excitonic linewidth in transition metal dichalcogenides
Zahra Khatibi, Maja Feierabend, Malte Selig, Samuel Brem, Christopher Linderälv, Paul

Erhart and Ermin Malic
2D materials **6**, 1 (2018)

Resistivity Anomaly in Weyl Semimetal candidate Molybdenum Telluride
Dhavala Suri, Christopher Linderalv, Bogdan Karpiak, Linnea Anderson, Sandeep Kumar Singh, Andre Dankert, F. C. Chou, Raman Sankar, F. C. Chou, Paul Erhart, Saroj P. Dash, R. S. Patel
arXiv:1801.05162 (2018)

Contents

1 Introduction 1
1.1 Outline of the thesis 2

2 Wide band gap oxides 3
2.1 Zaanen-Sawatsky-Allen theory 3
2.2 Alignment of band edges 4
2.3 Transparent conducting oxides 5
2.4 Multiferroics 7
2.5 Phosphors 8

3 Hexagonal boron nitride 11
3.1 Emission lines 12

4 Outline of defect physics 15
4.1 Point defects in crystals 16
4.2 Origin of point defect formation 17
  4.2.1 Configurational entropy 17
4.3 Formation energy of a defect 18
  4.3.1 Electron chemical potential 19
  4.3.2 Chemical potential 19
4.4 Shallow and deep defect levels 19
4.5 Defect level alignment 21
4.6 Transitions involving defect levels 21
  4.6.1 Electronic transitions 21
  4.6.2 Vibronic transitions 23
4.7 Experimental techniques for studying point defects 27

5 First-principles methodology 29
5.1 Density functional theory 30
  5.1.1 Kohn-Sham equations 30
  5.1.2 Exchange and correlation 31

5.1.3 Limitations of local and semi-local DFT 32
5.1.4 Modelling excited states 33
5.1.5 Modelling charged systems 33
5.2 Phonons 34
5.2.1 Local modes 35

6 Summary of the papers **37**
6.1 Paper I 37
6.2 Paper II 38
6.3 Paper III 38

7 Outlook for the future **39**

Acknowledgments **41**

Bibliography **43**

1

Introduction

The main topic of this thesis is the *interaction between charge and defects in insulators.* To understand why this is important, one can consider some of the energy related challenges that modern societies face. Arguably, the most urgent problems in order to transition to a sustainable society include improving energy efficiency in electronic and optical devices, improving efficiency of renewable energy harvesting, energy storage as well as control over chemical reactions. All these processes involve charge transport in one way or another. Wide band gap oxides are a very versatile class of material that contains compounds utilized (together with other materials) in all of these applications. The processes that these applications are founded upon are all influenced to some extent by crystalline defects including oxygen vacancies. For example, defects can capture mobile charge carriers, which results in a reduction of conductivity, or alter the electronic structure resulting in a different catalytic performance.

Energy related applications are perhaps the most urgent areas in which wide band gap oxides are used, but there are other fields as well in which wide band gap oxides are in demand. In microelectronics and optoelectronics, the relatively small band gap of semiconductors makes them far from the best performing material in all situations. For high power devices where the width of the band gap is important, attention has, however, been directed to semiconductors/insulators with a much wider band gap than what is typically found in semiconductors [1]. There is no universal wide band gap material such as silicon in the field of semiconductors. Rather there is a number of promising candidates that have been suggested. These candidates include nitrides such as $Al_xGa_{1-x}N$ and a number of wide band gap oxides such s Ga_2O_3. Defects are important in microelectronics as well, since in an application where high charge transport rates are important, a fundamental understanding of how these charges are affected by defects is important.

Defects are in many applications an undesired crystallographic irregularity that deteriorates the performance of a material. In some cases however, the presence of crystallographic irregularities is required in order to achieve desired performance. In particular, defects in wide band gap materials can host optical systems that can be utilized in, e.g., light emitting diodes and sensors. The gemstones ruby, sapphire, and emerald, to name a few, are simply transparent wide band gap oxides with transition metal impurities that alter the optical response.

While one can observe the macroscopic effects of defects, e.g., as a reduction in electrical conductivity, change in optical transmission or emission of light, a fundamental understanding of the underlying defective structure is almost always hampered by the difficulties in observing and monitor the relevant microscopic processes. Here *ab initio* modelling is an invaluable tool that allows us to study single defects and relate the findings to macroscopic phenomena.

In the following chapters, fundamental properties of oxygen vacancies in wide band gap oxides will be discussed as well as the role of oxygen vacancies in non-radiative recombination in wide band gap oxide based phosphors. Furthermore, the optical lineshape of point defect emission in boron nitride is addressed.

1.1 Outline of the thesis

In Chapter 2, *wide band gap oxides* are introduced, followed by highlighting a few areas where oxygen vacancies in wide band gap oxides can have a particularly large influence on the performance of the material. The optical properties of boron nitride is introduced in Chapter 3. Chapter 4 contains a technical outline of the physics of point defects starting with the thermodynamics of point defects. In the latter part of the chapter, electronic transitions on defects are discussed. The theory behind the computational methods used to obtain a quantitative description of the energetics of point defects is outlined in Chapter 5. The papers on which this thesis is based are summarized in Chapter 6. Finally, Chapter 7 is an outlook for the future.

2

Wide band gap oxides

Oxygen forms compounds with basically every other element in the periodic table, and even wide band gap oxides are a rather large class of oxides and not rigorously defined. For the present thesis, the class of wide band gap oxides is defined as crystalline oxides with band gaps above 3 eV.

The valence electron configuration of oxygen is $2s^2 2p^4$. In the *ionic limit* oxygen occurs in oxides as a doubly negatively charged ion with a closed valence shell $2s^2 2p^6$ when forming the oxide with metals. In *closed shell* oxides the metal ions have a depleted valence shell, which is reflected in the stoichiometry of the oxide. This entails that the valence band consists of localized oxygen p states and the conduction band of unoccupied metal states.

2.1 Zaanen-Sawatsky-Allen theory

The type of a semiconductor/insulator can be classified according to the predominant character of the valence and conduction band manifolds. While the degree of covalency can be large, it is still useful to keep the notion of anion and cation. In the case of binary compounds with ionic character, there is some degree of mixing between anion and cation states, however, it is usually possible to distinguish the *main* origin of the valence band and conduction band states. It is in that case possible to assign the valence band edge to either anion or cation valence states and the conduction band to cation valence states.

A semiconductor or insulator for which the valence band is dominated by anion states and the conduction band by cation state is said to be a charge transfer semiconductor or insulator. Here the “charge transfer” means that the lowest excitation requires a charge transfer between the anion and cation. When both valence and conduction band are derived from the cation states, the semiconductor or insulator is of Mott-Hubbard type and the lowest excitation involves charge transfer between cations.

In 1985, Zaanen, Sawatsky and Allen (ZSA) developed a theory in order to qualitatively understand the electronic structure of transition metal compounds applicable to binary transition metal oxides [2]. In ZSA theory the distinction between charge transfer and Mott-Hubbard insulators can be made. The theory is simple in the sense that it is based on only three material specific parameters to describe the type of insulator. The essence of ZSA theory is that the electronic properties of an ionic transition metal oxide are dependent on the charge transfer energy between the oxygen and metal states (δ) and the correlation energy between the metal states (U) (see illustration in Fig. 2.1). The third parameter entering the ZSA theory is the oxygen $2p$ band width W.

The band gap in Mott-Hubbard insulators arises due to *strong* correlation of the localized M-d states that suppresses charge transfer between metal atoms.

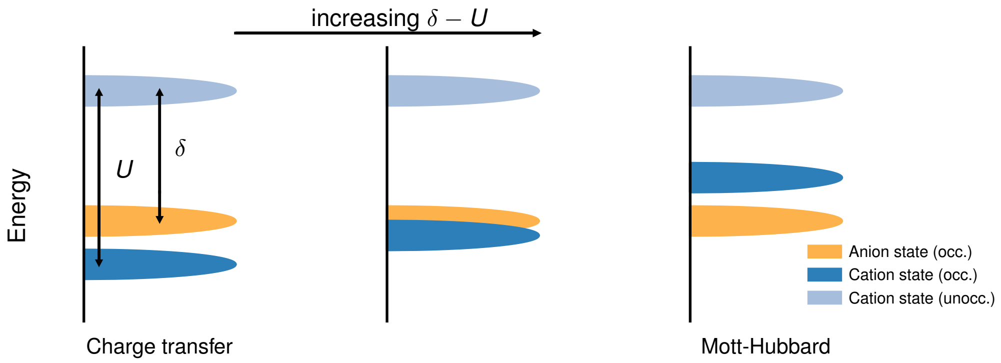

Figure 2.1: Illustration of the parameters for the ZSA theory. The band width W (not shown) of the oxygen $2p$ states is the width of the orange band. The difference between the band edge character in charge transfer insulators and Mott-Hubbard insulators is indicated.

Mott-Hubbard insulators have $\delta - U > 0$, while for charge transfer insulators $\delta - U < 0$. The binary transition metal oxides studied in the publications that this thesis is based on are closed shell charge transfer insulators. As such, the unoccupied metal states are usually well separated from the occupied oxide states, *i.e.* $U \gg \delta$ [3].

2.2 Alignment of band edges

The relative band edge positions between different materials are important in any device which includes a junction of these materials. Therefore, extensive efforts have been made in order to understand how band edges align. There are two main types of alignment, type I and type II, see illustration in Fig. 2.2a.

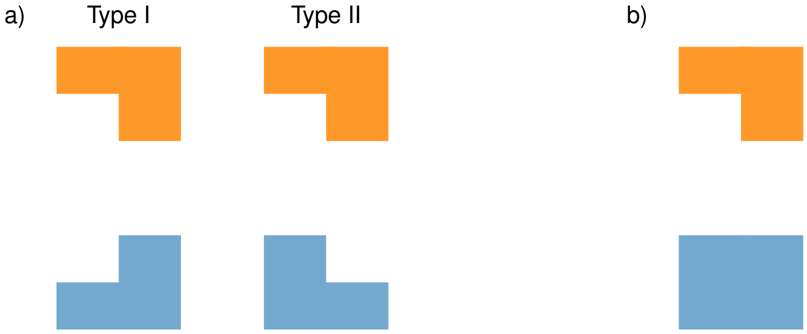

Figure 2.2: a) Illustration of Type I and Type II band alignment. b) Illustration of the common anion rule.

In binary ionic charge transfer semiconductors/insulators, the anion valence states are occupied and the cation valence states are unoccupied in the ground state. It has been observed that compounds with common anions tends to exhibit a much smaller variation of the valence band edge compared with the conduction band edge [4] (illustration in Fig. 2.2b). This observation is the basis of the so-called common anion rule.

The common anion rule states that the valence band edge position is *primarily* determined by the energy level of the anion valence state, whereas the conduction band edge position is primarily determined by the energy level of the cation valence state. Wei and Zunger showed that the common anion rule breaks down when metal states mixes with valence band edge states [5].

2.3 Transparent conducting oxides

Band gap materials usually exhibit either insulating behavior and transparency in the visual region of the electromagnetic spectrum (e.g., SiO_2) or semiconducting behaviour accompanied by absorption in the visual region (e.g., Si). There are, however, materials that exhibit both of these features at the same time. In order for a material to be transparent in the visual region of the spectrum, the *optical* band gap has to be larger than slightly above 3 eV. The large band gap impedes the intrinsic formation of free charge carriers, which prevents high intrinsic charge carrier mobility. Electrical conduction in certain wide band gap oxides is possible to achieve by doping the oxide. In order to maintain the transparency with a large concentration of free charge carriers, the free charge carrier absorption must exhibit a small spectral weight in the visual part of the spectrum. It has been noted that the optical band gap can be quite a lot larger than the electronic (or transport) band gap due to forbidden transitions between the band edges [6].

Transparent conducting oxides (TCOs) are a loosely defined class of oxides that exhibit both transparency in the visual region of the spectrum and conduct electricity. Examples of oxides that fall in the class of TCOs are ZnO, TiO_2, In_2O_3, SnO_2, β-Ga_2O_3, $BaSnO_3$ as well as $CuAlO_2$. The valence band of binary charge transfer TCOs is predominantly composed of oxygen $2p$ states while the conduction band consists of metal states. In complex TCOs such as $CuAlO_2$, significant hybridization of metal states with the valence band can occur [7].

The industrial standard TCO is the In-Sn oxide alloy (ITO) [8]. The conduction band of the constituent oxides (In_2O_3 and SnO_2) consists of s states, which are highly dispersive suggesting that the electron mobility can be high due to low electron effective masses. In fact, ITO exhibits an electron mobility of 30 $cm^2/(Vs)$ and solar transmittance of 80% [9]. However, due to the technological importance of indium (e.g., ITO), demand has risen substantially over the last couple of decades and concerns about long term supply have been raised [10]. In light of this, alternatives to ITO are evaluated. In this regard, Al doped ZnO (AZO) is a promising material that consists of abundant, cheap, and non-toxic materials and could replace ITO [8].

2.3.0.1 Role of defects

In order to take full advantage of a TCO, one needs to construct interfaces between n and p doped regions (pn-junctions), and so far it has been difficult to achieve both n and p type doping in the same material. TCOs are generally n-doped and realizing p-doping has been a long standing research goal. The origin of the preferred n-doping over p-doping is believed to be related to the formation of oxygen vacancies which act as an electron donor in all TCOs, though the donor efficiency of the oxygen vacancy varies between materials [11].

The main difficulties involved in utilizing p-doped oxides can be understood by first considering the O^{2-} ion, which is a closed shell ion and is unlikely to want to host a free hole. Secondly, if one manages to form O^- ions, hole capture by occupied abundant intrinsic hole killers reduce the hole concentration. Finally, even if a TCO with a valence band of $2p$ states e.g. ZnO and In_2O_3 could be easily p-doped, the effective mass of the hole is usually very large due to the localization of the oxygen $2p$ states. In a band diagram, the valence band in these materials is very flat. Hence, the free hole mobility for the cases where the valence band edge consists of oxygen $2p$ states is very low limiting the usefulness in electrical devices [12, 13]. It has also been shown that holes may form small polarons (self trapped holes) in the TCOs SnO_2, Ga_2O_3 and In_2O_3, which further reduces the hole mobility [14] in these materials.

Intrinsic hole killers in TCOs have been widely studied. For example, in the case of ZnO, intrinsic defects have been suggested to be the source of the difficulty in achieving a *p*-doped material. The difficulty arises from an asymmetry between acceptor and donor defects in terms of formation energy that is independent of chemical potential [15]. It is shown that hole killers such as V_O are abundant while electron killers are rare under growth conditions, thus achieving *n*-type doping is easier based on intrinsic compensating defects.

There are, however, TCOs that can easily be made to exhibit hole conductivity. In the TCOs $CuMlO_2$ (M=Al, Ga, In), the cation valence states (Cu *d* states) overlap significantly with the oxygen $2p$ states, effectively inducing a curvature of the valence band and therefore creating a reasonable conduction channel for holes [7].

2.3.0.2 Applications

The main properties of TCOs that are attractive in applications are obviously optical transparency and electrical conductivity. There is, however, a large set of applications where only the electrical conductivity is important.

TCOs are used in photovoltaic devices and flat panels as transparent electrodes where both transparency and conductivity is important. The TCO is used as a current collector (anode) at the front-end (illuminated) side of a photovoltaic device.

Furthermore, for next generation microelectronics wide band gap oxides have suitable properties. β-Ga_2O_3 (monoclinic phase) has a band gap of 4.8 eV. In fact, together with SiC (3.3 eV) and GaN (3.4 eV), TCOs such as ZnO and β-Ga_2O_3 are considered candidates for high-power semiconductor devices due to the large band gap and the possibility to achieve electronic conduction [16, 1]. The reason that these wide band gap materials are considered for electronic devices is that these materials can sustain a much larger electric field before break-down than regular semiconductors.

2.4 Multiferroics

Ferroelectricity is a property of some polar materials that contains a non-zero reversible polarization without any applied electric fields much like ferromagnets exhibit a magnetic ordering without applied magnetic fields. While polar materials exhibit non-zero polarization, it is in general not reversible. The ability to switch the polarization between two states by an applied electric field has led to the use of ferrolectric materials in certain computer memory technologies (so called FeRAM).

Multiferroics is a class of materials that exhibit either two or three out of ferroelectricity, ferromagnetism, and ferroelasticity simultaneously [17]. Certain oxides such as $BiFeO_3$, $BaMnO_3$, and $YMnO_3$ are among the most promising multiferroic materials. Compound materials consisting of a perovskite ferroelectric such as $BaTiO_3$ and a ferromagnetic material are also being considered [18].

Oxygen vacancies in ferroelectric materials have been shown to contribute to ferroelectric fatigue in the material, i.e., the polarization as a function of switches between the different states decay [19, 20, 21]. That is, oxygen vacancies dictate the lifetime of the ferroelectric performance of the material. Oxygen vacancies are readily formed in perovskite oxides and while the oxygen vacancy distribution is random at low concentration, clustering can occur at larger oxygen vacancy concentration [19, 22]. The clustering of oxygen vacancies can interact with domain walls, rendering domain walls immobile, which leads to suppression of the polarization switching.

2.5 Phosphors

A crystalline phosphor is a crystal with discrete electronic energy levels that can host an optical transition by spontaneous emission from a higher occupied state to a lower unoccupied state.

In general, a crystalline phosphor is composed of two components, a host matrix and an activator ion. A wide band gap of the host matrix is required in order for optical transitions to occur without populating/depopulating band states, which can deteriorate the optical performance of the phosphor. One of the most important oxide-based phosphors is Ce doped yttrium aluminium garnet (YAG). Other host matrices, e.g., $Lu_3Al_5O_{12}$ (LuAG) have, however, also found widespread use in solid state lighting applications.

The stoichiometry of YAG is $Y_3Al_5O_{12}$ and it is together with yttria aluminia perovskite (YAP) the most important oxide of Y and Al. The oxide parent phases Y_2O_3 and Al_2O_3 are wide band gap oxides with band gaps of 5.6 eV and 7.0 eV, respectively. The space group of YAG is $Ia\bar{3}d$. It is a cubic structure with a conventional unit cell that consists of 160 atoms. The YAG crystal can be described in terms of oxygen coordination of Al and Y atoms. Al exists in two symmetry inequivalent positions. The Al atom is the center atom in both an octahedron and an tetrahedron formed by oxygen atoms. The Y atom is coordinated to 8 oxygen atoms, and is the center of a dedocrahedon. The band gap of YAG has been estimated to values between 6.4 eV [23] and 7.7 eV [24].

The technological importance of YAG is exclusively as a host matrix in solid state lighting applications as it can be doped by quite a few elements in the Lanthanide series. The lanthanide contraction makes the ionic radius of the early lanthanides (115 pm to 113 pm) compatible with substitution on the Y site (ionic radius of 104 pm). The most common substitutional elements are Ce, which together with YAG results in a yellow phosphor, and Nd, which together with YAG can be used as an infrared laser.

The inclusion of Ce in YAG has the effect that the Ce $4f$ and $5d$ states fall between the band edges of pristine YAG. A schematic illustration is shown in Fig. 2.3.

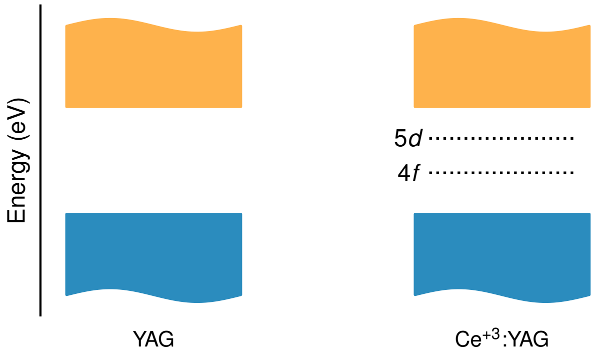

Figure 2.3: Schematic illustration of the ideal YAG band structure and the band structure of Ce:YAG.

The electronic transitions $4f^1 5d^0 \leftrightarrow 4f^0 5d^1$ are the basis of down-converting blue light to yellow light. The mechanism underlying the down-conversion is that when the electron configuration changes, as it does when a photon is absorbed or emitted, the equilibrium ion positions changes, which in turn changes the relative potential energy between the ground and excited state. The relative potential energy is the transition energy, i.e. the frequency of the emitted photon. The basic principle behind a w-LED based on down conversion is that a blue light emitter such as GaN or $\mathrm{In}_x\mathrm{Ga}_{1-x}\mathrm{N}$ emits photons through Ce:YAG [25], which overlaps with the absorption frequency in Ce:YAG. A fraction of the blue photons will be down-converted to photons centered at the yellow region of the visual spectrum by the optical transition and a fraction will pass through the material. The resulting mixture of blue and the down converted light is perceived as white light.

2.5.0.1 Luminescence quenching

Luminescence quenching is the observed luminescence intensity decay, which can result from external operating conditions such as elevated temperature or due to operation at high power. Instead of recombining radiatively, a fraction of the generated electron-hole pairs recombines non-radiatively. Ce:YAG exhibits luminescence quenching with increasing temperature, which sets limits to the maximal operating temperature. The luminescence quenching as a function of activator ion concentration was studied by Bachmann *et al.* [26], where it was found that for 3.3% doped Ce:YAG, luminescence quenching is already present at 300 K. Furthermore, the temperature for onset of luminescence quenching decreases with increasing activator ion concentration.

There are numerous mechanisms that can lead to luminescence quenching, including the following, which have been suggested to be important in Ce:YAG: thermal crossover of potential energy landscapes, concentration quenching and ionization of the excited state. The concentration quenching mechanism is a mechanism in which the initial excitation energy migrates through the lattice until it reaches a killer center (see Fig. 2.4). Concentration quenching is dependent on the concentration of the activator ions but also on the presence of killer centers i.e. defects. The initial excitation energy can be transferred between an excited state Ce ($4f^05d^1$) atom and a ground state Ce atom ($4f^15d^0$) by resonant energy transfer

$$\mathrm{Ce}^* + \mathrm{Ce} \rightarrow \mathrm{Ce} + \mathrm{Ce}^*. \tag{2.1}$$

Resonant energy transfer is possible if the two species Ce and Ce* interact via exchange interaction or if there is a spectral overlap of the absorption and emission bands i.e radiation trapping. Exchange interaction requires overlapping wave functions. While energy can be transferred between ions up to distances of about 10 Å [27], the efficiency of energy transfer has a $\boldsymbol{R}^{-6}$ dependence on the distance between the activator ions. The excitation energy is eventually transferred to a killer center that transforms the excitation energy to heat.

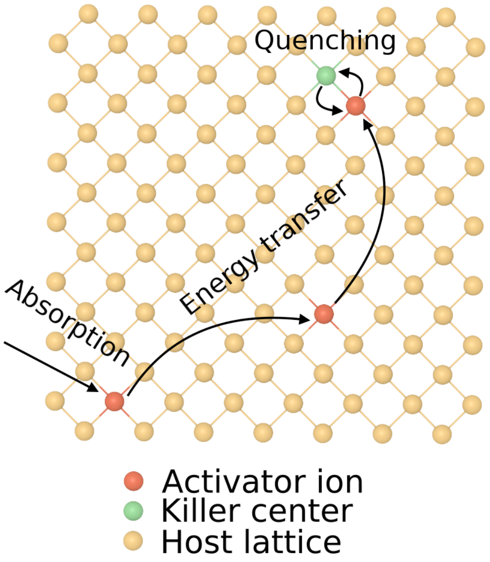

Figure 2.4: Illustration of the concentration quenching mechanism.

3

Hexagonal boron nitride

Boron nitride (BN) exhibits, similar to carbon, different crystal structures depending on temperature and pressure. The most stable structure of BN at ambient conditions is a hexagonal layered structure that is similar to graphite. The structure consists of layers with hexagonal symmetry in which B and N are covalently bonded (Fig. 3.1). The individual layers interact via van-der-Waals forces. At higher pressures, a diamond like structure exists as well.

Monolayer hexagonal BN (h-BN) has received a lot of attention after the fabrication of graphene, and mono and few-layer h-BN can be fabricated with similar methods as graphene, i.e., mechanical exfoliation and chemical vapor deposition.

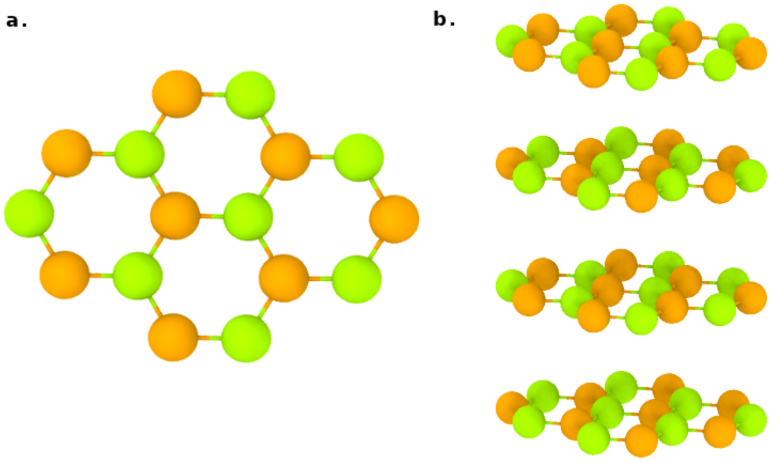

Figure 3.1: a) In-plane structure of h-BN. b) Bulk structure of h-BN.

The electronic structure of h-BN is, however, very different from graphene. In contrast to graphene, the monolayer of h-BN is a wide band gap material with a band gap of 6 eV [28]. Due to the large band gap of h-BN, one of the main applications of h-BN is as a substrate material in 2D heterostructures where the structural compatibility with graphene is the major advantage over more conventional insulating substrates such as silica.

h-BN can, however, also be used as a 2D or quasi-2D host matrix for optical systems due to the large band gap. In 2015, it was found that both monolayer and bulk h-BN can exhibit bright quantum emission at optical wavelengths [29], a feature that was also shown for emission centers in the UV region [30].

Due to the reduced dimensionality, photon sources in 2D materials do not inherently suffer from the same limitations as photon sources in bulk 3D materials. For example, emission from localized sources in 2D materials does not exhibit total internal reflection to the same degree as in 3D. Furthermore, manipulation of the crystal structure on the atomic level is easier on the surface of a material than manipulation at specific sites within bulk materials, which could enable more precise control over the emission energy.

3.1 Emission lines

After the discovery of quantum emission in h-BN, it was rapidly established that there was a large variation in the emission energies. It was found that emission at optical wavelengths occurs at discrete values in the range between 1.6 eV and 2.3 eV. In Fig. 3.2, the emission lineshape of a few emitters are shown.

Furthermore, these emitters in the 1.6 eV-2.3 eV band were spatially localized, which suggest that optical transitions on defects are a likely origin. Photoluminesence measurements show that many of these defects exhibit similar emission line shapes. For example, there is often a single pronounced peak in the side band at 165 meV below the zero phonon line (ZPL) (Fig. 3.2), which has been attributed to the emission of a phonon.

From experiments, quite a lot is known about these emission centers although their precise structure is unknown. First, the emission lifetime is very short, on the order of 1 ns. The short lifetime of the excited state suggests that band states are likely not involved since the delocalized nature of the band states leads to a much smaller transition dipole moment, which governs the lifetime. Secondly, the temperature stability of the emission center is high and room temperature emission can be observed, which suggests that the levels are well separated from the band edges.

Initially, the nitrogen vacancy (V_N) and the N_B-V_N defect were advocated as possible sources [33]. C_B-V_N has also been suggested as a possible source [36].

In addition to the 1.6 eV-2.3 eV emission band, there is a well known emission energy

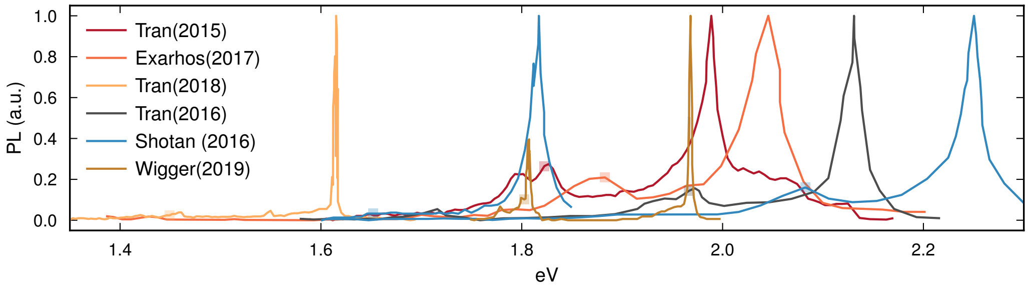

Figure 3.2: Experimentally measured photoluminescence curves extracted from Tran(2015)[29], Exarhos(2017)[31], Tran(2018)[32], Tran(2016)[33], Shotan(2016)[34] and Wigger(2019)[35].

at 4.1 eV. It has been suggested that this emission energy corresponds to a transition on C_N, and more recently to be the result of a transition on the C-C dimer (C_N-C_B) [37]. In **Paper III** the emission lineshapes of point defect emitters in h-BN are studied.

4

Outline of defect physics

Having seen some implications of defects in wide band gap oxides and hexagonal boron nitride, this section contains a more detailed discussion of defect physics with an emphasis on defects in materials with a band gap.

In metals, where the Fermi level is positioned within a partially filled band, the modification of the electronic level structure by the introduction of a point defect typically does not induce any localized single particle states. While the defect level may perturb the single particle wave function of a charge carrier close to the Fermi level, it still maintains its delocalized character. While the defect perturbs the wave function, it may have profound effects on transport properties, e.g., electronic and thermal transport by inducing additional scattering channels of charge carriers and phonons.

In contrast to defects in metals, defects in semiconductors and insulators can, due to the band gap, trap charge carriers in spatially localized defect levels and hence exhibit different charge states. In an insulator, an induced defect level can fall within the band gap (while it is common, it is not general). The energy level difference between the band states and the defect level ensures that the *single particle* wave function of the charge carrier trapped at a defect level is spatially localized. The degree of localization depends on host material and defect type.

In order to facilitate communication of defect physics, a modified Kröger-Vink notation is adopted here. The notation is based on the introduction of a defect A at site B. The symbol A may be a chemical symbol, e.g., in substitutional defects or a V that indicates that the defect is a vacancy. An atom of species Mo that substitutes for a W atom is denoted as $\mathrm{Mo_W}$. A vacancy of species O is denoted as $\mathrm{V_O}$. The charge state of the defect is reported in the usual way, e.g., a doubly positive charged vacancy of species A is denoted as $\mathrm{V_A^{+2}}$ and a neutral substitutional defect where B substitutes for A is denoted as $\mathrm{B_A}$. In Kröger-Vink notation the charge states would be reported as follows: $\mathrm{B_A} \rightarrow \mathrm{B_A^{\times}}$, $\mathrm{B_A^{+1}} \rightarrow \mathrm{B_A^{\bullet}}$ and $\mathrm{B_A^{-1}} \rightarrow \mathrm{B_A^{\prime}}$.

4.1 Point defects in crystals

The ideal lattice structure, with infinite repetition of smaller units is only an approximation of the crystal used in a laboratory or in an industrial setting. This approximation is in most cases sound, when modelling properties such as structural, vibrational or electronic bands in high quality crystals. There are a few situations, which are sometimes predominantly governed by the defects in the crystal. For example, luminescence, mass transport, charge carrier concentrations, and mobility in doped semiconductors to name a few.

Point defects can be grouped in intrinsic and extrinsic defects. An intrinsic defect can be found in a pure material, while an extrinsic defect requires foreign atom species. Extrinsic defects are sometimes referred to as impurities and are easier to control than intrinsic defects. In Fig. 4.1, an illustration of some of the most common point defects is shown. These defects include

a. vacancy (intrinsic)

b. interstitial (intrinsic, extrinsic)

c. antisite (intrinsic)

d. substitutional defect (extrinsic).

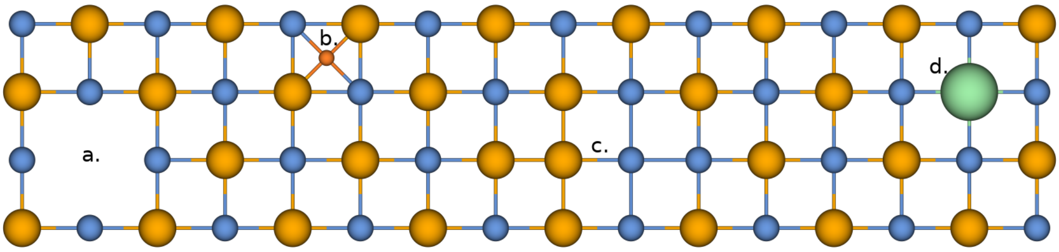

Figure 4.1: Schematic illustration of common point defects in solids. a is a vacancy, b is an interstitial, c is an antisite defect and d is a substitutional defect.

Introducing substitutional defects is sometimes referred to as *doping*, e.g., in the case of Ce doping in YAG, a Ce atom substitutes for a Y atom. Point defects can also be more complicated such as a combination of the above mentioned point defects. Examples include

A Frenkel defect is a vacancy-interstitial pair.

Various forms of topological defects e.g. Stone-Wales defects. These defects are stoichiometric but involve a change of connectivity and are associated with very large formation energies.

Split interstitial configurations where an interstitial atom share a lattice point with the same atoms.

Vacancy substitutional complexes such as the NV-center in diamond, which is a pair consisting of a vacancy and a nitrogen substitutional defect.

Naturally, there is a large diversity in the possible point defects in a material.

4.2 Origin of point defect formation

4.2.1 Configurational entropy

All crystals will almost always contain some non-zero concentration of point defects due to the increase of configurational entropy that comes with addition of defects. Point defects are zero-dimensional defects that consists of a deviation from the ideal structure at a single or a few lattice points.

If the crystal is finite and contains N sites, introducing a single *single site* defect will dramatically lower ΔG at any finite temperature. The number of ways n defects can be distributed among N sites is $\begin{pmatrix} N \\ n \end{pmatrix} = \frac{N!}{n!(N-n)!}$. If a crystal with zero defect interaction is considered, the entropy is $S = k_b \ln(W)$, with W = $\begin{pmatrix} N \\ n \end{pmatrix}$, since the energy of the system is independent of the location of the defects due to non interacting defects. The increase in entropy of adding defects in the dilute defect limit $N/n \to \infty$ is dramatic since the derivative of the configurational entropy with respect to number of defects is ∞ at the dilute limit. One can explicitly compute the $\partial_n S$ by using Stirling's formula ($Q! = Q(\ln(Q) - 1)$ for $Q >> \ln(Q)$) assuming that both n and N are sufficiently large.

The entropy S is then obtained by applying Stirling's formula to $S = k_b \ln\left(\frac{N!}{n!(N-n)!}\right)$

$$S = k_b[N\ln(N) - n\ln(n) - (N-n)\ln(N-n)], \tag{4.1}$$

and

$$\partial_n S = k_b \ln\left(\frac{N}{n} - 1\right), \tag{4.2}$$

which tends to infinity in the dilute limit.

Due to the large number of sites N involved in any practical crystal, the concentration of point defects is non-zero. Finite and possibly low dimensional systems on the other hand is not subjected to the same increase in configurational entropy.

4.3 Formation energy of a defect

The formation of defects is governed, just like any chemical reaction, by the free energy. However, entropic contributions are small at low temperatures and do not change the qualitative behaviour of a defect at least at low temperatures.

The formation energy of a point defect is a measure of the energetic cost for creating a defect. The formation energy of an electrically neutral vacancy in a monoatomic system, with chemical potential from the same phase can be computed as

$$\Delta E_F = E(N-1) - \frac{N-1}{N} E(N), \tag{4.3}$$

where N is the number of atoms in the computational cell. In semiconductor, a defect can exists in different charge states depending on the electrochemical potential. The formation energy of a point defect in a polyatomic system in charge state q can be defined as [38]

$$\Delta E_F^q = E_{\text{def}}^q - E_{\text{ideal}} - \sum_i \Delta n_i \mu_i + q(\varepsilon_{\text{VBM}} + \Delta \mu_e), \tag{4.4}$$

where E_{def}^q is the total energy of the defect cell in charge state q. E_{ideal} is the total energy of the ideal cell. $\Delta n_i \mu_i$ is the change in numbers of species i with chemical potential μ_i. Finally, E_{VBM} is the valence band maximum and $\Delta \mu_e$ is the relative electron chemical potential. The formation energy of a defect is usually positive, since a negative value suggests that spontaneous formation of defects would take place, i.e., the pristine structure is unstable at 0 K with respect to defect formation.

The formation energy is a central quantity since it can be associated with the equilibrium defect concentration via the expression

$$c = g \exp\Big(-\frac{\Delta E_F}{k_B T}\Big), \tag{4.5}$$

where g is the density of defect sites. The formation energy dependence on the charge state of the defect allows for analyzing the equilibrium charge state of a defect. The charge transition level (CTL) is the value for the electron chemical potential at which there is a transition in equilibrium charge state of a defect. This transition occurs when the formation energies of two charge states are the same. For the CTL between a neutral and a doubly positively charged defect

$$0 = \Delta E_{\text{f}}^{q=0} - \Delta E_{\text{f}}^{q=+2}, \tag{4.6}$$

leads to

$$\varepsilon(0/+2) = \frac{E_{\text{def}}^{q=0} - E_{\text{def}}^{q=+2}}{2} - \varepsilon_{\text{VBM}}. \tag{4.7}$$

4.3.1 Electron chemical potential

The electron chemical potential $\Delta\mu_e$ that appears in Eq. 4.4 is not a free parameter but is fixed by charge neutrality conditions. The charge state of some defects can be controlled by applying external fields which has been shown to be possible in the case of NV-centers in diamond [39].

In equilibrium the electron chemical potential depends on *all* possible defects. By knowledge of all formation energies and density of defect sites Eq. 4.5 can be used to compute the electron chemical potential together with the charge carrier concentrations that are given by

$$n_e = \int_{\varepsilon_{\mathrm{CBM}}}^{\infty} d\varepsilon g(\varepsilon) f_F(\varepsilon; \mu, T) \tag{4.8}$$

$$n_h = \int_{-\infty}^{\varepsilon_{\mathrm{VBM}}} d\varepsilon g(\varepsilon)[1 - f_F(\varepsilon; \mu, T)], \tag{4.9}$$

where g is the density of states and f_F is the Fermi-Dirac distribution i.e. $f_F(\varepsilon; \mu, T) = [1 + \exp[(\varepsilon - \mu)/kT]^{-1}$. Eq. 4.5, together with Eq. 4.8 - 4.8 are solved self-consistently to find the electron chemical potential and the equilibrium charge state for a system containing defects.

4.3.2 Chemical potential

The chemical potential μ_i of element i in Eq. 4.4 depends on the environment from which element i is taken. The elemental phases provides an upper bound of the energy so that Eq. 4.4 is stoichiometric but will in most cases not provide useful information about the relevant formation energies. Instead, in order to obtain relevant formation energies, the chemical potential should resemble the external conditions.

In the case of an oxide exchanging oxygen atoms with a gas containing oxygen (such as air), the chemical potential of oxygen can be related to the partial pressure of the oxygen gas [38]

$$\mu_{\mathrm{O}} = \frac{1}{2} E_{\mathrm{O}_2} + \frac{kT}{2}\Big(\ln\Big[\frac{Ph^3}{kT[2\pi mkT]^{3/2}}\Big] - \ln Z_{\mathrm{rot}} - \ln Z_{\mathrm{vib}} \Big), \tag{4.10}$$

where Z_{rot} and Z_{vib} are the rotational and vibrational partition functions respectively.

In the case of binary compounds such as BN the equilibrium conditions of the crystal implies that the chemical potentials of the constituent species are coupled

$$\mu_{\mathrm{B}} + \mu_{\mathrm{N}} = E(BN). \tag{4.11}$$

4.4 Shallow and deep defect levels

The position of the charge transition level within the band gap determines the ionization energy of a localized electron (donor defect) or localized hole (acceptor defect).

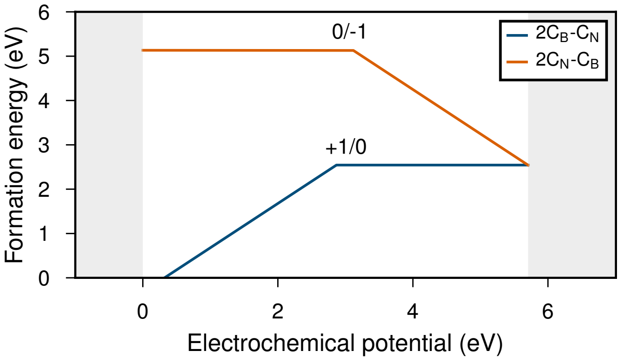

Figure 4.2: Formation energy of a deep donor (blue line) and a deep acceptor (red line).

The fraction of defects that are ionized in equilibrium is determined by Fermi-Dirac statistics. An occupied state within the band gap is a shallow donor state if it is easily ionized, i.e. it donates the electrons to the conduction band. Similarly, an unoccupied state close to the valence band is a shallow acceptor state if valence band electrons are easily transferred to the acceptor state, i.e. the acceptor state donates holes to the valence band.

Deep defect states on the other hand are formed well below the conduction band (or well above the valence band) such that the fraction of ionized defects is close to zero for all relevant temperatures. In Fig. 4.2 the formation energy of a deep acceptor level and a deep donor levels is shown. Deep defect states cannot be used for improving the electrical conductivity of a material, and furthermore the deep defect states can enhance the electron-hole recombination rate, which effectively destroys free charge carriers via Shockley-Read-Hall recombination. Since shallow and deep defects have fundamentally different influence on a material it is important to be able to distinguish between the two. Efforts to understand why oxygen vacancies are shallow in some materials have been undertaken. In Ref. [40] it was suggested that the shallow/deep character of an oxygen vacancy in a wide band gap oxide was determined by the character of the conduction band minimum. Oxides for which the conduction band minimum was derived from antibonding cation-anion states e.g. ZrO_2, ZnO, SnO_2, In_2O_3 exhibit deep neutral oxygen vacancies. For oxides where the conduction band minimum was derived from cation-anion non-bonding states, the oxygen vacancy was shallow e.g. TiO_2.

4.5 Defect level alignment

It has been shown that some defect levels exhibit more or less constant values with respect to the vacuum level across a wide variety of materials. Universality of defect level position was experimentally shown for transition metal impurities in compound III-V semiconductors [41]. The idea that these deep defect levels were vacuum derived due to the material independence instead of derived from valence or conduction band states of the host was forwarded. It was later shown by Caldas [42] via first-principles calculations that the charge transition level of several transition metal impurities exhibited a constant value over the III-V compound semiconductors when referred to the vacuum level. Here, the width of the distribution of the defect level was attributed to the covalency of the host material. Recently, Dorenbos showed that the vacuum referred binding energy of the Ti +4/+3 charge transition level exhibited relatively small variations in a wide range range of oxides [43].

Besides transition metal impurities, universality of defect levels has been shown for the hydrogen +1/-1 charge transition level in a variety of insulating materials including some oxides [44]. In **Paper I** it is shown that the oxygen vacancy +2/0 charge transition level exhibits small variation across a series of wide band gap oxides with varying band gaps and different crystal structures.

The interest in defect level alignment is many-fold. From a fundamental point of view, the alignment of defect levels casts doubt on the opinion that the defect level is derived from the host band edge states due to the independence of the band edge positions. Furthermore, chemical trends across host materials may become more transparent. From a practical point of view, if used for extrapolation educated estimates of the position of a defect level may be made without explicitly computing it, which can be useful in materials screening.

4.6 Transitions involving defect levels

4.6.1 Electronic transitions

Radiative transitions can occur between two defect bound states, i.e., between two localized states, or between a localized state and a band state, which is a delocalized state. An example of a radiative transition between two localized states is the $4f \leftrightarrow 5d$ transition on the Ce atom in Ce:YAG. An example of a localized state to a delocalized state transition is the photoionization of a deep oxygen vacancy in a wide band gap oxide

$$\mathrm{V}_{\mathrm{O}}^{q=0} + \hbar\omega \rightarrow \mathrm{V}_{\mathrm{O}}^{+1} + e'_{\mathrm{CBM}}. \tag{4.12}$$

The transition energy in the absence of a change in vibrational state for a transition that involves a localized and a delocalized state can be related to the equilibrium charge

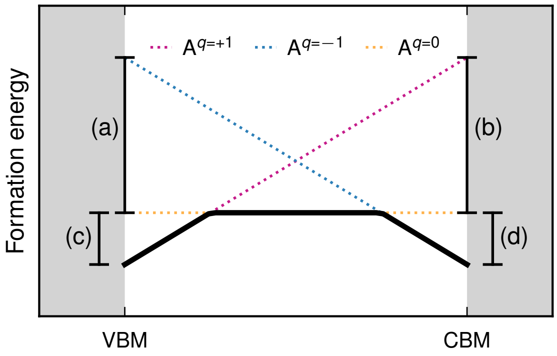

Figure 4.3: Electronic transition associated with a charge state change on the defect. Here the defect is labelled with A and can exhibit the charge states +1, 0 and -1. The transitions (a), (b), (c) and (d) corresponds to charge carrier capture from band states. See the text for a description of these transitions.

transition level. In Fig. 4.3 the formation energy of a defect labelled A is shown that can exist in the charge states -1,0 and +1. In this case there are four possible transitions involving band states. These transitions are labelled (a) through (d) in Fig. 4.3. The transition (a) corresponds to VBM hole capture on $A^{q=-1}$. The transition (b) corresponds to a CBM electron capture on $A^{q=+1}$. The transition (c) corresponds to a VBM hole capture on $A^{q=0}$ and transition (d) corresponds to a CBM electron capture on $A^{q=-1}$.

In order for an electronic transition to be allowed, the transition dipole moment between the initial and final state must be non zero. The lifetime of the excited state is also partially governed by the magnitude of the transition dipole moment via the Einstein A coefficient. This can be explained by considering the time dependence of the absolute state occupancy of the excited state

$$\frac{dn(t)}{dt} = -An(t), \tag{4.13}$$

that is, the excited state occupancy is proportional to the number of excited states. The differential equation has the solution

$$n(t) = n(t = 0)\exp(-At) \tag{4.14}$$

The quantity A here is the the Einstein A coefficient and is related to the spontaneous emission rate as

$$\tau = \frac{1}{A}. \tag{4.15}$$

The Einstein A coefficient can be expressed in terms of the transition dipole moment and zero phonon line of a transition as [45]

$$A = \frac{e^2 \omega_{\mathrm{ZPL}}^3 \mu^2}{3\pi \epsilon_0 \hbar c^3}. \tag{4.16}$$

The radiative lifetime decreases with increasing value of the transition dipole moment and increasing transition energy.

A transition between a localized and a delocalized state usually has a shorter lifetime than a localized-localized transition. This difference originates in the generally smaller spatial overlap of the initial and final wave functions due to delocalization of one of the involved states.

4.6.2 Vibronic transitions

A vibronic transition is an electronic state transition that is accompanied by a vibrational state transition. The reaction for emission of a photon is

$$E_{\mathrm{initial}} + \sum_i n_{i,\mathrm{initial}} \hbar\omega_{i,\mathrm{initial,phonon}} \rightarrow E_{\mathrm{final}} + \sum_j n_{j,\mathrm{final}} \hbar\omega_{j,\mathrm{final,\ phonon}} + \hbar\omega_{\mathrm{photon}}, \tag{4.17}$$

as it proceeds from left to right. Here n_i is the phonon occupation number of mode i and E is the potential energy associated with the electronic state. Vibronic transitions are a consequence of the coupling between electronic and vibrational degrees of freedom, which gives rise to additional structure in optical lineshapes.

An electronic transition on a defect is *always* accompanied by a change of the atomic geometry. This can be explained by the fact that the final state is subject to a different potential due to reorganization of charge than the the initial state and therefore subject to orbital relaxation that leads to ionic reorganization. For example, in the case of the $4f \leftrightarrow 5d$ transition in Ce:YAG, the spatial extension of the $5d$ state is much larger than the extension of the $4f$ state, which implies different local potentials. The effect may be even larger in the case of a localized-delocalized transition where the localization of charge can induce rather large structural differences e.g. in the case of photoionization of an oxygen vacancy.

The atomic geometry distortion is connected to the energy dissipation ΔE that occurs when the system relaxes to the vibrational ground state. This process is called vibrational relaxation and is a fast process that occurs during a time span on the order of 10^{-12} s in most materials. The magnitude of the atomic geometry distortion over the electronic transition can be characterized by

$$\Delta Q_{\mathrm{if}}^2 = \sum_{a=1}^{N} m_a \Delta \boldsymbol{R}_a \cdot \Delta \boldsymbol{R}_a, \tag{4.18}$$

where $\Delta\boldsymbol{R}_a$ is the position difference between the initial and final state of atom a.

A simple model that can be used to describe a vibronic transition is the 1D configuration coordinate diagram [46], here illustrated in Fig. 4.4. The potential energy surface of an electronic state, which is a function of all the ionic degrees of freedom is projected onto a single coordinate, which is called a configuration coordinate. This configuration coordinate is obtained by interpolating the ionic positions between the initial state and final state. Effectively creating an *effective phonon mode* that describes the ionic motion between the equilibrium geometry of the initial state and final state.

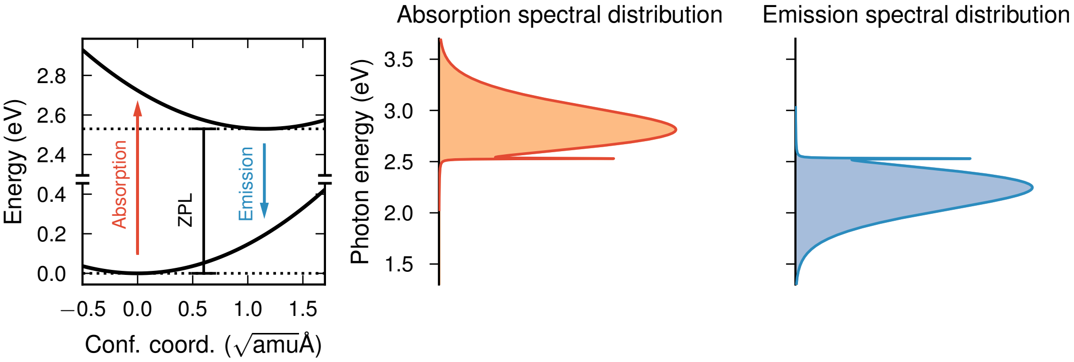

Figure 4.4: Illustration of the vibrational coupling of electronic transitions that results in phonon sidebands for the case of the $4f \leftrightarrow 5d$ transition on Ce in Ce:YAG.

The frequency ω_{eff} of the effective phonon mode is determined by the curvature of the potential energy along the configuration coordinate. The quantity

$$S = \frac{\Delta E}{\omega_{\mathrm{eff}}} = \frac{1}{2}\omega_{\mathrm{eff}}\Delta Q_{\mathrm{if}}^2 \tag{4.19}$$

is called the Huang-Rhys factor. The last equality holds in a perfectly parabolic potential energy surface. The ω_{eff} of the initial and final potential energy surface does not need to agree. In the case where the ω_{eff} are the same, the Huang-Rhys factor is related to the Stokes shift as

$$\Delta E_{\mathrm{Stokes}} = 2\omega_{\mathrm{eff}} S. \tag{4.20}$$

Here the Stokes shift is the difference between the absorption energy peak and the emission energy peak. An interpretation of the Huang-Rhys factor, which is transparent from eq. 4.19 is that it is the *number* of effective phonon modes emitted in a vibronic transition. The 1D configuration coordinate model can provide insight to a vibronic transition and provide numerical values of measurable quantities that are characteristic for the vibronic transition e.g. ZPL, $\Delta E_{\mathrm{Stokes}}$, S and Debye-Waller factor. The drawback of this model is that it does not contain information about the specific phonon modes that are involved in the transition, which are required in order to resolve the structure of the phonon sidebands. Therefore, this model is not suitable for a deeper investigation of a vibronic transition.

4.6.2.1 Generating function method

The generating function method is a feasible approach to evaluate the rate of a vibronic transition that can be applied to both radiative transitions and non-radiative transitions. The generating function method was developed in the early 1950's by Melvin Lax [47] and further studied by Kubo, Toyozawa [48] and Markham [49]. Since then this method has made its way to electronic structure calculations and with high-performance computer systems it has been shown to be able to accurately describe the spectral lineshape of radiative transitions [50] and capture cross-sections for non-radiative transitions [51].

The normalized radiative emission intensity and excitation intensity can be expressed as [52, 53]

$$A(\omega) = N_A \omega F(\omega) \tag{4.21}$$

$$E(\omega) = N_E \omega^3 F(\omega), \tag{4.22}$$

where N_A and N_E are normalization constants and $F(\omega)$ is given by

$$F(\omega) = \sum_{\nu_1,\nu_2} n_s |\langle \Psi_{f,\nu_2}(q,Q)| \boldsymbol{M} |\Psi_{i,\nu_1}(q,Q)\rangle|^2 \delta(\Delta\omega_{if} - \omega), \tag{4.23}$$

where Ψ_{f,ν_2} is the vibronic wave function indexed by quantum numbers f that indicates the electronic state and ν_2 that indicates the vibrational state and similarly for Ψ_{i,ν_1}. $\boldsymbol{M}$ is the transition dipole moment operator $e\boldsymbol{r}$ and n_s is the Boltzmann population $\exp(\varepsilon/[k_b T])/Z$ where Z is the partition function. q is the electronic coordinate and Q is the ionic coordinate. In the generating function method F can be expressed as the Fourier transform of the generating function

$$F(\omega) = \frac{1}{2\pi} \int_{\infty}^{\infty} dt G(t) \exp(i\omega t), \tag{4.24}$$

In general G is a quite complicated function. For vibronic transitions on defects in solids one typically has to impose several approximations in Eq. 4.23 such as the Franck-Condon approximation, parallel mode approximation and the low temperature approximation [50].

The Franck-Condon approximation states that transitions occur vertically on the potential energy surfaces and that the transition dipole moment is independent of atomic coordinates. This approximation is intimately connected to the Born-Oppenheimer approximation and builds upon the same foundation i.e. the electron dynamics is much faster than the ion dynamics.

The parallel mode approximation simplifies the problem significantly by assuming that the vibrational properties of the ground state and the excited state are *exactly* the same. This is of course never true, and may be a quite severe approximation in the case of electronic transitions with very large atomic geometry difference and/or different symmetries between the initial and final states. The implication of this approximation is that the normal modes of the initial and final states are related simply by an affine transformation. In the cases were the parallel mode approximation does not hold, the normal modes are not simply related by an affine transformation, but a rotation as well resulting in a transformation of the following form

$$\boldsymbol{Q}_f = \boldsymbol{J}\boldsymbol{Q}_i + \boldsymbol{K}. \tag{4.25}$$

In the Franck-Condon approximation, parallel mode approximation and the assumption that the transition occurs from the vibrational ground state of the initial electronic state the generating function attains a simple form. The following approach to evaluate the optical lineshapes within these approximations was formulated by Alkauskas *et al.* [50] and builds on earlier work of Miyakawa and Dexter [53]. The first step in order to arrive at a model that accounts for the contribution of specific phonon modes is the mode decomposition of the Huang-Rhys factor

$$S = \sum_{\nu=1}^{3N} s_\nu, \tag{4.26}$$

where s_ν is the *partial* Huang-Rhys factor defined as

$$s_\nu = \frac{1}{2}\omega_\nu \Delta \boldsymbol{Q}_\nu^2. \tag{4.27}$$

Here ω_ν is the energy of phonon mode ν and $\Delta \boldsymbol{Q}_\nu$ is now the projection of the atomic coordinate difference $\Delta \boldsymbol{R}$ on the normalized phonon displacement vector $\boldsymbol{n}_\nu$ as

$$\Delta Q_\nu = \sum_{n=1}^{N} \sqrt{m_n} \Delta \boldsymbol{R}_a \cdot \boldsymbol{n}_{\nu,a} \tag{4.28}$$

The partial Huang-Rhys factors are then used to create the electron phonon spectral function defined as

$$D(\omega) = \sum_\nu s_\nu \delta(\omega - \omega_\nu) \tag{4.29}$$

The generating function is then

$$G(t) = \exp\left[\int_0^\infty D(\omega)\exp[-i\omega t] d\omega - S\right]. \tag{4.30}$$

The δ functions in Eq. 4.29 are in practice approximated by normalized Gaussian functions with a smearing of a few meV.

In smaller systems such as molecules the low temperature approximation, parallel mode approximation and the Franck-Condon approximation may not be required in order to model the optical lineshapes. In the work by Baiardi, Bloino, and Barone [52] the solution to Eq. 4.23 beyond the Franck-Condon, parallel mode and low temperature approximations is outlined.

4.7 Experimental techniques for studying point defects

The macroscopic effect of point defects on materials can be significant so that the presence of defects can be inferred easily. However, characterizing the defect by element, type and the energy position of the level is very challenging. Furthermore, most experimental techniques have been developed with small band gap semiconductors (i.e. silicon) in mind and the extension to wide band gap materials is not always straightforward.

One of the most common experimental techniques for probing deep charged defects in semiconductors is deep-level transient spectroscopy (DLTS) [54]. The principle behind DLTS is to form a depletion region and measure the capacitance, which is different between a localized and delocalized state. From a DLTS measurement one can extract information about activation energy for thermal ionization, concentration and capture cross sections as well as the acceptor vs. donor character. The extraction of the activation energy is usually done by repeating the measurement at different temperatures and make a fit to an Arrhenius function. It has been shown that any comparison between standard theoretical predictions of ionization energy of a defect and DLTS will suffer from temperature effects which may be prominent [55]. Since its invention in 1974, DLTS has successfully been utilized to study defects in semiconductor materials such as Si and GaN. However, probing oxygen vacancies in wide band gap oxides is much more challenging due to difficulties forming the required *pn*-junction in many oxides and the deepness of the oxygen vacancy state in many wide band gap oxides.

DLTS can only probe defects with a maximal deepness of around 1 eV since the transition is temperature induced, thus not suitable for deep oxygen vacancies in many wide band gap oxides and many other defects in insulators, which entails additional considerations. In the case of deep defects $>$ 1 eV, the electronic transition can be induced by light pulses [56]. Since only the capacitance is measured, the method does not provide information about the elements that induce the defect state.

Photoluminesence measurements may also be used to probe optically active defects such as activator ions in wide band gap oxides. In essence, the material under study is subjected to photons of a specific wavelength which causes electronic excitations in the material. The emission spectra upon the return to ground state is recorded. Here information about the zero phonon line and the positions of the sidebands can be obtained. If the optical transition involves free band states the energy position of the defect level can be extracted.

5

First-principles methodology

In order to study equilibrium properties of point defects from first-principles, a parameter free method to compute the total energy of a system is required to obtain predictive results. The method must be sufficiently cheap since the first principles methodology for defect thermodynamics is based on the study of large systems. Density functional theory is an approximate parameter free method that combines predictive power and computational feasibility. In what follows, the relevant elements of density functional theory are outlined.

The starting point is the Hamiltonian describing a system of electrons and atoms (in atomic units $\{\hbar = 1, m_e = 1, e = 1, \epsilon_0 = 1/(4\pi)\}$)

$$\begin{aligned} H(r,R) = -\frac{1}{2}\sum_{k=1}^{N}\frac{\nabla_k^2}{M_k} - \frac{1}{2}\sum_{i=1}^{n}\nabla_i^2 + \frac{1}{2}\sum_{i=1}^{n}\sum_{j=1,j\neq i}^{n}\frac{1}{|r_i - r_j|} - \sum_{i=1}^{n}\sum_{k=1}^{N}\frac{Z_k}{|r_i - R_k|} + \\ + \frac{1}{2}\sum_{k=i}^{N}\sum_{l=1}^{N}\frac{Z_k Z_l}{|R_l - R_k|} \end{aligned} \tag{5.1}$$

In order to simplify Eq. 5.1, the first approximation that is performed is the separation of the ionic and electronic subsystems. This is the adiabatic approximation, or Born-Oppenheimer approximation which is justified by the fact that the proton mass is much heavier than the electronic mass. Formally, in the adiabatic approximation, the combined ion and electron wavefunction factors

$$\psi(r,R) = \psi_e(r)\psi_n(R). \tag{5.2}$$

The Hamiltonian in Eq. 5.1 can be decomposed in an electronic, ionic and interaction part

$$H(r,R) = H_{el}(r) + H_{ion}(R) + H_{el-ion}(r,R) \tag{5.3}$$

$$H_{el}(r) = -\frac{1}{2}\sum_{i=1}^{n}\nabla_i^2 + \frac{1}{2}\sum_{i=1}^{n}\sum_{j=1,j\neq i}^{n}\frac{1}{|r_i - r_j|} \tag{5.4}$$

$$H_{ion}(R) = -\frac{1}{2}\sum_{k=1}^{N}\frac{\nabla_k^2}{M_k} + \frac{1}{2}\sum_{k=i}^{N}\sum_{l=1}^{N}\frac{Z_k Z_l}{|R_l - R_k|} \tag{5.5}$$

$$H_{el-ion}(r, R) = -\sum_{i=1}^{n}\sum_{k=1}^{N}\frac{Z_k}{|r_i - R_k|} \tag{5.6}$$

The H_{el} acts only on the electronic part of the wavefunction, while the H_{ion} only acts on the ionic part of the wavefunction. The interaction term can be parameterized in ionic coordinates R so that the equation that has to be solved is

$$\left(-\frac{1}{2}\sum_{i=1}^{n}\nabla_i^2 + \frac{1}{2}\sum_{i=1}^{n}\sum_{j=1,j\neq i}^{n}\frac{1}{|r_i - r_j|} - \sum_{i=1}^{n}\sum_{k=1}^{N}\frac{Z_k}{|r_i - R_k|}\right)\psi(r; R) = \varepsilon(R)\psi(r; R) \tag{5.7}$$

for a given ionic configuration R. Hence, the wavefunction and the energy depends on the ionic positions parametically.

5.1 Density functional theory

Density functional theory (DFT) is in principle an exact theory for the electronic subsystem that can tackle eq. 5.7 by reformulating the equation in terms of electron density rather than wave functions.

DFT is based on the Hohenberg-Kohn theorems [57]. The first Hohenberg-Kohn theorem states that the external potential, which provides a setting for the electronic subsystem is uniquely determined by the *ground state* electron density. The second Hohenberg-Kohn theorem is an existence theorem of an energy functional. The energy functional is such that it exhibits a global minimum only for the ground state electron density.

5.1.1 Kohn-Sham equations

The Hohenberg-Kohn theorems are fundamental but gives no direction on how to obtain the ground state energy of the electronic subsystem. The *Kohn-Sham approach* is to reformulate the interacting many electron system to many non-interacting electron systems, effectively constructing a mean field theory. The Kohn-Sham equation is [58]

$$\left(-\sum_{i=1}^{N}\frac{\nabla_i^2}{2} + V_{\text{eff}}\right)\phi_i = \varepsilon_i\phi_i. \tag{5.8}$$

Here ϕ_i is a *single* particle Kohn-Sham state. The Kohn-Sham equation is non-linear due to the dependence of the effective potential V_{eff} on the Kohn-Sham states. The effective potential contains the following terms

$$V_{\textbf{eff}} = V_{\text{ext}} + V_H + V_{XC} \tag{5.9}$$

where V_H is the Hartree potential and V_{XC} is the so called exchange-correlation potential, which is the challenging part. V_{ext} is the external potential seen from the electrons point of view, i.e. the ions. The effective potential depends on the electron density. The electron density is constructed from orthonormal single-particle Kohn-Sham states as

$$n(r) = \sum_{i=1}^{N} f_{nk} |\phi_{nk}|^2. \tag{5.10}$$

f_{nk} are occupation numbers and in principle only occupied states are required to obtain the ground state energy. In practice, empty bands are included for two main reasons, some numerical procedures are more stable with empty states and sometimes an interpretation of Kohn-Sham states are made. This could be the band gap for example. Note that the Kohn-Sham states are electronic states for the reformulated equation and hence have no rigorous physical significance. Due to the non-linear nature of Eq. 5.8, it is solved self-consistently.

5.1.2 Exchange and correlation

5.1.2.1 Local and semi-local functionals

The simplest method to account for exchange correlation interactions in DFT is by treating the exchange correlation (XC) within the local density approximation (LDA) [57]. In LDA the XC energy is a functional of the electron density only, which is a local quantity. LDA typically predict shorter binding lengths compared with experiments and suffers in system where the electron density is changing rapidly.

One extension to LDA is to include information about how the the electron density changes. This results in a class of functionals called generalized gradient approximation (GGA) and sometimes referred to as semi-local functionals. In GGA functionals the XC energy is a function of the electron density and the gradient magnitude of the electron density. The GGA functionals can be parameterized in several ways resulting in different GGA functionals, e.g. PBE[59].

Van der Waals (vdW) interactions are not captured by standard local or semi-local XC functionals. A number of XC functionals that account for vdW interactions has been developed such as vdW-DF-cx [60]. Functionals that account for vdW interactions are essential in order to describe some wide band gap oxides such as MoO_3, which crystallizes in a layered structure.

While accounting for vdW interactions is absolutely necessary in some materials e.g. layered materials, it has been found that vdW-DF-cx describes the structural properties e.g. lattice parameters in an excellent manner even in solids that are not classified as vdW solids [61].

5.1.3 Limitations of local and semi-local DFT

Local and semi-local DFT both exhibits spurious self-interaction i.e. an electron interacts with itself via the mean field. This is referred to as the self-interaction error (SIE) and is a significant drawback of local and semi-local DFT. The SIE is responsible for the excessive delocalization of single particle states. The SIE makes it difficult to describe systems with very localized electronic states e.g. f states and some defect states such as polaron states. The SIE can be compensated to some extend by adding a Coulomb repulsion on localized states using the Hubbard-U model. Furthermore, local and semi-local DFT tend to underestimate the band gap significantly.

Another remedy for the SIE is the usage of hybrid functionals. Including part of the exact exchange in the potential energy of a Kohn-Sham system results in a class of functionals termed *hybrid functionals*. In the simplest case, the exchange correlation energy can be written as

$$E_{\mathrm{XC}}^{\mathrm{hybrid}} = E_{\mathrm{C}}^{l/sl} + \alpha E_{\mathrm{X}}^{HF} + (1-\alpha) E_{\mathrm{X}}^{l/sl}, \tag{5.11}$$

where s/sl denotes local/semi-local and α is the mixing parameter usually taken as 1/4 [62]. It is however not uncommon to tune the mixing parameter to match experimental band gaps. Hybrid functionals comes with a larger computational cost due to the evaluation of the two-center integrals of the form

$$K_{nk,mk'} = \int drdr' \frac{n^{\dagger}_{nk,mk'}(r) n_{nk,mk'}(r')}{|r-r'|}, \tag{5.12}$$

where $n_{nk,mk'}(r) = \phi_{nk}(r)\phi^{\dagger}_{mk'}(r)$. The energy position of the valence band maximum and conduction band minimum as computed with hybrid functionals are still not physical in general, but the difference is often in better agreement with experiments, resulting in a much better description of the band gap. While certain defect levels may delocalize under local and semi-local DFT, localized levels on the local and semi-local level of theory is already properly described [63] compared with a description on the hybrid level of theory if a common reference level is used.

There are several different hybrid functionals. For crystalline systems the two most popular hybrid functionals are PBE0 [62, 64] (Eq. 5.11) and HSE06 [65, 66], the latter includes screened exchange.

5.1.4 Modelling excited states

DFT is a ground state theory and makes no assertions of excited states. The naive method to approach excited state quantities such as transition energies is to consider the Kohn-Sham state energy difference. This is typically what is done when evaluating the band gap of a material with DFT although that quantity involves excited state quantities. Aside from the fact that the Kohn-sham states are not proper quasi-particles, the main error in this approach when modelling transitions that involves a defect state is that the same local potential is used to describe both the ground and excited state. In fact, during an electronic transition involving a localized state the local potential changes. If one consider the $4f - 5d$ transition in Ce doped YAG, the ground state potential account for the population of the $4f$ state but not of the $5d$ state.

A better approximation is to work with total energy differences and constrain the state occupations and evaluate the energy self-consistently with fixed occupations. In the case of Ce doped YAG, the excited state state would have a depleted $4f$ manifold and one occupied $5d$ state. This approach is called ΔSCF. ΔSCF accounts for the difference in local potential between the excited and ground state and thus also the lattice configuration difference. Accounting for the lattice configuration difference is essential in order to model quantities that involves the coupling between electronic states and vibrational degrees of freedom such as non-radiative transition rates and vibrational broadening of optical spectra.

While ΔSCF is a phenomenological approach to extend the reach of DFT, the method has been shown to yield accurate transition energies in the case of the NV^{-1} center in diamond [50] and transitions on activator ions in lanthanide doped phosphors [67].

5.1.5 Modelling charged systems

Models of crystalline systems require periodic boundary conditions. While a real crystal is charge neutral on average, theoretically one can consider charged systems by modifying the number of electrons. The standard method to avoid a divergence in the electrostatic energy is to add a compensating background charge based on the Jellium model so that the computational cell is charge neutral. Localized charge will however still interact with its periodic image. This will have the effect that the formation energy of a localized charged defect is dependent on the size of the system beyond elastic interactions, which entails additional considerations when modelling the dilute limit formation energy of a charged defect. The finite size effect has two contributions, *i*) image charge interactions, *ii*) inconsistent reference levels due to different external potentials and different charge.

Methods to account for image charge interactions has been developed based on the monopole and multipole interactions and Lany and Zunger suggested the following form of the image charge correction [68]

$$E_C = \frac{Mq^2}{3L\varepsilon}, \tag{5.13}$$

where M is the Madelung constant.

In order to account for the inconsistent reference levels, the potentials of the ideal and defect cells have to be aligned. To see where the potential difference arises one can consider the relevant terms in in Eq. 4.4 and the reference potentials (here denoted with V_i for potential of the pristine cell and V_d for the defect cell).

$$\Delta E_F^q = \overbrace{E_{\text{def}}^q}^{V_d} - \overbrace{E_{\text{ideal}}}^{V_i} + q(\overbrace{\varepsilon_{\text{vbm}}}^{V_i}) \tag{5.14}$$

From the expression above it is clear that the electron chemical potential and the energy from the charged defect are not referenced to the same reference potential. A potential alignment term ΔV that accounts for the potential difference between the ideal cell and the charged defect cell has to be added. In practice, the alignment of the potential between a charged system and the ideal system can be done by considering the difference in average electrostatic potential far from the defect. Charge neutral defects also exhibits inconsistent reference levels due to the different external potential.

For 2D systems with partially screened and unscreened interactions a correction scheme was developed by Komsa based on the notion of special vacuum [69, 70].

5.2 Phonons

The vibrational properties of a crystal, such as frequencies and corresponding vibrational eigenbasis of can be obtained semi-classically, which is justified based on the ion mass, by a series expansion. The total energy is parametically dependent on the ionic positions (in the Born-Oppenheimer approximation) so a series expansion in ionic displacements can used to map out the potential energy landscape as a function of ionic positions.

The series expansion to first non-vanishing order can be written as

$$E = \frac{1}{2}\sum_{i\alpha,j\beta} \frac{\partial E^2}{\partial u_i^\alpha \partial u_j^\beta} \delta u_i^\alpha \delta u_j^\beta, \tag{5.15}$$

where the zero energy level is the ground state energy and since it is in equilibrium, the forces (i.e. first order term) vanishes. The indices i, j runs over ions and α, β over spatial components. The quantity $\Phi_{i,j}^{\alpha,\beta} = \frac{E^2}{\partial u_i^\alpha \partial u_j^\beta}$ is called a force constant. The force constants are related to the equations of motions for the ions through the *dynamical* *matrix*, which is obtained by mass weighting the Fourier transform of the real space force constants.

$$D^{\alpha,\beta}_{i,j}(q) := \frac{1}{\sqrt{M_i M_j}} C^{\alpha,\beta}_{i,j}(q) = \sum_k \Phi^{\alpha,\beta}_{i,j} \exp(-iqr_k) \tag{5.16}$$

The equations of motions are then found by diagonalizing the dynamical matrix

$$\boldsymbol{D}^{\alpha,\beta}_{i,j}(q)\boldsymbol{\varepsilon}_{\nu,\boldsymbol{q}} = \omega^2_{\nu,\boldsymbol{q}}\boldsymbol{\varepsilon}_{\nu,\boldsymbol{q}}. \tag{5.17}$$

The $\varepsilon_{\nu,q}$ is the normalized phonon eigenvector of branch ν at position q in reciprocal space.

The force constants can be evaluated by making small displacements of the ions and recording the total energy. Expanding the total energy of a crystal in a power series require a certain smoothness of the total energy as a function of the ionic coordinates in order for the power series to converge. In 3D polar materials, there is a long range electrostatic interaction that leads to the the splitting of the longitudinal and transversal optical modes at the zone center.

5.2.1 Local modes

A local mode is a mode where typically only a few atoms participate in the collective motion. As such, the dispersion in reciprocal space is flat. A mode can be shown to be a local mode by considering the inverse participation ratio defined by Alkauskas *et al.* [50] as

$$\mathrm{IPR}_\nu = \frac{1}{\sum_a (\Delta\boldsymbol{R}_{\nu,a} \cdot \Delta\boldsymbol{R}_{\nu,a})^2} \tag{5.18}$$

and the dependence on supercell size. Here $\Delta\boldsymbol{R}_{\boldsymbol{\nu}}$ is a normalized displacement vector and ν is a mode index and a is an atom index. In the most local case one can think of, i.e. one atom that constitutes the whole displacement vector, the IPR_ν is one. For translational modes the IPR_ν is the number of atoms in the computational cell [50].

6

Summary of the papers

6.1 Paper I

Paper I deals with general properties of oxygen vacancies in wide band gap oxides, e.g., TCOs and ferroelectric oxides. Here, the charge transition level (CTL), lattice distortion, and Kohn-Sham eigenvalues associated with the oxygen vacancy in 26 wide band gap oxides are studied.

We show that the CTLs between the neutral and doubly ionized oxygen vacancy state only show minor variations over a range of wide band gap oxides with band gaps that vary between 3 eV and 9 eV. We show this by aligning the band edges of the pristine oxides so that the CTLs have a common reference point. We find that the average value of the CTL is -5.7 eV with respect to the vacuum level and the standard deviation is 0.35 eV, which is a relatively small variation in light of the magnitude of the band gap variations.

The charge associated with the neutral oxygen vacancy is in the case of deep states predominantly localized in the vacancy cavity and the CTL does not change significantly between semi-local DFT and hybrid functionals if the state is already localized on the level of semi-local DFT. We find that the structural relaxation due to charge state change is significant and an accurate indicator of the character (*deep vs. shallow*) of the oxygen vacancy. The Kohn-Sham eigenvalue corresponding to the defect state is located in the forbidden gap and also serves as an indicator of a deep state.

The results can be used for estimating the character of an oxygen vacancy by only knowing the band edge position of the pristine crystal. Here the the position of the conduction band minimum with respect to the vacuum level determines the character of the oxygen vacancy.

6.2 Paper II

In **Paper II** we assess the role of oxygen vacancies in luminescence quenching in Ce:YAG. We show that the oxygen vacancy defect state is deep and cannot be identified with electronic states that trap electrons from the conduction band commonly found in Ce:YAG.

We propose a charge transfer mechanism where the excitation energy is eventually dissipated to lattice vibrations due to a charge state change on an oxygen vacancy. While the forward reaction exhibits favorable energetics, in order to recycle the oxygen vacancy as a recombination center hole capture on the vacancy is required. We find that the charge transfer energy barrier is still lower than for other mechanisms for luminescence quenching.

In **Paper II**, we furthermore study the vibrational fine structure of the optical lineshape for the Ce:$4f - 5d$ transition. We find that the fine structure in absorption and emission spectra cannot be associated with a single local mode. Instead, the fine structure is the result of coupling between the electronic transition and many delocalized phonon modes.

6.3 Paper III

In **Paper III**, point defect emission in monolayer h-BN is investigated. The formation energies and charge transition levels of the most common intrinsic defects and carbon based defects are studied. The formation energies suggest that carbon based defects where a carbon substitutes for B and N are associated with much smaller formation energies than the intrisic defects. In order to assess the potential of these defects to act as emission centers with a narrow emission and large intensity of the zero phonon line the defects are screened based on the magnitude of lattice distortion.

For the defects with small lattice displacements between excited and ground states, the emission line shape is computed and it is revealed that the only intrinsic defect that can be responsible for the 1.6-2.3 eV emission line is V_B. Furthermore, we find that the carbon based defects C_N, C_B and C_N-C_B exhibit structured lineshapes that can be associated with experimentally found lineshapes of observed emission centers.

7

Outlook for the future

Oxygen vacancies are such an abundant point defect in many technologically important materials, but the role of oxygen vacancies in recombination and charge carrier scattering is largely unknown. The role of oxygen vacancies on recombination processes was started in the study of luminescence quenching in Ce:YAG but there are open questions e.g. the charge carrier capture rate on the oxygen vacancies which is important for the process proposed in **Paper II**. Investigating the charge carrier capture rates on oxygen vacancies in wide band gap oxides would be beneficial for the understanding of scattering mechanisms in conducting oxides as well as recombination rates.

Acknowledgments

I wish to express my gratitude towards my main supervisor Paul Erhart for sharing his enthusiasm about unsolved problems in physics that has allowed me to work in diverse areas of materials physics. Furthermore, I like to thank my co-supervisors Mikael Kuisma and Ermin Malic for sharing their knowledge about excitons in 2D materials. I would also like to thank Daniel Åberg for introducing me to the field of vibrational coupling to defects. Finally I would like to thank all past and present members of the research group.

Bibliography

[1] J. Y. Tsao, S. Chowdhury, M. A. Hollis, D. Jena, N. M. Johnson, K. A. Jones, R. J. Kaplar, S. Rajan, C. G. Van de Walle, E. Bellotti, C. L. Chua, R. Collazo, M. E. Coltrin, J. A. Cooper, K. R. Evans, S. Graham, T. A. Grotjohn, E. R. Heller, M. Higashiwaki, M. S. Islam, P. W. Juodawlkis, M. A. Khan, A. D. Koehler, J. H. Leach, U. K. Mishra, R. J. Nemanich, R. C. N. Pilawa-Podgurski, J. B. Shealy, Z. Sitar, M. J. Tadjer, A. F. Witulski, M. Wraback, and J. A. Simmons, *Ultrawide-Bandgap Semiconductors: Research Opportunities and Challenges*, Advanced Electronic Materials **4**, 1600501 (2018).

[2] J. Zaanen, G. A. Sawatzky, and J. W. Allen, *Band gaps and electronic structure of transition-metal compounds*, Physical Review Letters **55**, 418 (1985).

[3] J. B. Torrance, P. Lacorre, C. Asavaroengchai, and R. M. Metzger, *Why are some oxides metallic, while most are insulating?*, Physica C: Superconductivity **182**, 351 (1991).

[4] A. Klein, *Energy band alignment at interfaces of semiconducting oxides: A review of experimental determination using photoelectron spectroscopy and comparison with theoretical predictions by the electron affinity rule, charge neutrality levels, and the common anion rule*, Thin Solid Films **520**, 3721 (2012), 7th International Symposium on Transparent Oxide Thin Films for Electronics and Optics (TOEO-7).

[5] S.-H. Wei and A. Zunger, *Calculated natural band offsets of all II–VI and III–V semiconductors: Chemical trends and the role of cation d orbitals*, Applied Physics Letters **72**, 2011 (1998).

[6] A. Walsh, J. L. F. Da Silva, S.-H. Wei, C. Körber, A. Klein, L. F. J. Piper, A. DeMasi, K. E. Smith, G. Panaccione, P. Torelli, D. J. Payne, A. Bourlange, and R. G. Egdell, *Nature of the Band Gap of* In_2O_3 *Revealed by First-Principles Calculations and X-Ray Spectroscopy*, Physical Review Letters **100**, 167402 (2008).

[7] H. Kawazoe, M. Yasukawa, H. Hyodo, M. Kurita, H. Yanagi, and H. Hosono, *P-type electrical conduction in transparent thin films of* $CuAlO_2$, Nature **389**, 939 (1997).

[8] S. C. Dixon, D. O. Scanlon, C. J. Carmalt, and I. P. Parkin, *n-Type doped transparent conducting binary oxides: an overview*, Journal of Materials Chemistry C **4**, 6946 (2016).

[9] I. Hamberg and C. G. Granqvist, *Evaporated Sn-doped* In_2O_3 *films: Basic optical properties and applications to energy-efficient windows*, Journal of Applied Physics **60**, R123 (1986).

[10] L. Ciacci, T. T. Werner, I. Vassura, and F. Passarini, *Backlighting the European Indium Recycling Potentials*, Journal of Industrial Ecology **23**, 426 (2019).

[11] P. Ágoston, K. Albe, R. M. Nieminen, and M. J. Puska, *Intrinsic n-Type Behavior in Transparent Conducting Oxides: A Comparative Hybrid-Functional Study of* $\mathrm{In_2O_3}$, $\mathrm{SnO_2}$*, and ZnO*, Physical Review Letters **103**, 245501 (2009).

[12] K. H. L. Zhang, K. Xi, M. G. Blamire, and R. G. Egdell, *P-type transparent conducting oxides*, Journal of Physics: Condensed Matter **28**, 383002 (2016).

[13] H. Hosono and K. Ueda, *Transparent Conductive Oxides*, in *Springer Handbook of Electronic and Photonic Materials*, edited by S. Kasap and P. Capper (Springer International Publishing, Cham, 2017), pp. 1–1.

[14] J. B. Varley, A. Janotti, C. Franchini, and C. G. Van de Walle, *Role of self-trapping in luminescence and p-type conductivity of wide-band-gap oxides*, Physical Review B **85**, 081109 (2012).

[15] S. B. Zhang, S.-H. Wei, and A. Zunger, *Intrinsic n-type versus p-type doping asymmetry and the defect physics of ZnO*, Physical Review B **63**, 075205 (2001).

[16] H. W. Xue, Q. M. He, G. Z. Jian, S. B. Long, T. Pang, and M. Liu, *An Overview of the Ultrawide Bandgap* Ga_2O_3 *Semiconductor-Based Schottky Barrier Diode for Power Electronics Application*, Nanoscale Research Letters **13**, 1 (2018).

[17] H. Schmid, *Multi-ferroic magnetoelectrics*, Ferroelectrics **162**, 317 (1994).

[18] N. A. Spaldin and R. Ramesh, *Advances in magnetoelectric multiferroics*, Nature Materials **18**, 203 (2019).

[19] W. Li, A. Chen, X. Lu, and J. Zhu, *Collective domain-wall pinning of oxygen vacancies in bismuth titanate ceramics*, Journal of Applied Physics **98**, 024109 (2005).

[20] J. F. Scott and M. Dawber, *Oxygen-vacancy ordering as a fatigue mechanism in perovskite ferroelectrics*, Applied Physics Letters **76**, 3801 (2000).

[21] C. A.-P. de Araujo, J. D. Cuchiaro, L. D. McMillan, M. C. Scott, and J. F. Scott, *Fatigue-free ferroelectric capacitors with platinum electrodes*, Nature **374**, 627 (1995).

[22] A. I. Becerro, C. McCammon, F. Langenhorst, F. Seifert, and R. Angel, *Oxygen vacancy ordering in $CaTiO_3$–$CaFeO_{2.5}$ perovskites: From isolated defects to infinite sheets*, Phase Transitions **69**, 133 (1999).

[23] G. A. Slack, D. W. Oliver, R. M. Chrenko, and S. Roberts, *Optical Absorption of* $\mathrm{Y_3Al_5O_{12}}$ *from 10- to 55 000-*$\mathrm{cm^{-1}}$ *Wave Numbers*, Physical Review **177**, 1308 (1969).

[24] L. Ning, X. Ji, Y. Dong, W. Jin, Y. Huang, Z. Pan, and P. A. Tanner, *First-principles study of Ce-doped $Y_3Al_5O_12$ with Si–N incorporation: electronic structures and optical properties*, Journal of Materials Chemistry C **4**, 5214 (2016).

[25] J. McKittrick and L. E. Shea-Rohwer, *Review: Down Conversion Materials for Solid-State Lighting*, Journal of the American Ceramic Society **97**, 1327 (2014).

[26] V. Bachmann, C. Ronda, and A. Meijerink, *Temperature Quenching of Yellow Ce^{3+} Luminescence in YAG:Ce*, Chemistry of Materials **21**, 2077 (2009).

[27] G. Blasse and B. Grabmaier, *Luminescent Materials* (Springer-Verlag, Berlin Heidelberg, 1994).

[28] C. Elias, P. Valvin, T. Pelini, A. Summerfield, C. J. Mellor, T. S. Cheng, L. Eaves, C. T. Foxon, P. H. Beton, S. V. Novikov, B. Gil, and G. Cassabois, *Direct band-gap crossover in epitaxial monolayer boron nitride*, Nature Communications **10**, 2639 (2019).

[29] T. T. Tran, K. Bray, M. J. Ford, M. Toth, and I. Aharonovich, *Quantum emission from hexagonal boron nitride monolayers*, Nature Nanotechnology **11**, 37 (2016).

[30] R. Bourrellier, S. Meuret, A. Tararan, O. Stéphan, M. Kociak, L. H. G. Tizei, and A. Zobelli, *Bright UV Single Photon Emission at Point Defects in h-BN*, Nano Letters **16**, 4317 (2016).

[31] A. L. Exarhos, D. A. Hopper, R. R. Grote, A. Alkauskas, and L. C. Bassett, *Optical Signatures of Quantum Emitters in Suspended Hexagonal Boron Nitride*, ACS Nano **11**, 3328 (2017).

[32] T. T. Tran, M. Kianinia, M. Nguyen, S. Kim, Z.-Q. Xu, A. Kubanek, M. Toth, and I. Aharonovich, *Resonant Excitation of Quantum Emitters in Hexagonal Boron Nitride*, ACS Photonics **5**, 295 (2018).

[33] T. T. Tran, C. Elbadawi, D. Totonjian, C. J. Lobo, G. Grosso, H. Moon, D. R. Englund, M. J. Ford, I. Aharonovich, and M. Toth, *Robust Multicolor Single Photon Emission from Point Defects in Hexagonal Boron Nitride*, ACS Nano **10**, 7331 (2016).

[34] Z. Shotan, H. Jayakumar, C. R. Considine, M. Mackoit, H. Fedder, J. Wrachtrup, A. Alkauskas, M. W. Doherty, V. M. Menon, and C. A. Meriles, *Photoinduced Modification of Single-Photon Emitters in Hexagonal Boron Nitride*, ACS Photonics **3**, 2490 (2016).

[35] D. Wigger, R. Schmidt, O. D. Pozo-Zamudio, J. A. Preuß, P. Tonndorf, R. Schneider, P. Steeger, J. Kern, Y. Khodaei, J. Sperling, S. M. de Vasconcellos, R. Bratschitsch, and T. Kuhn, *Phonon-assisted emission and absorption of individual color centers in hexagonal boron nitride*, 2D Materials **6**, 035006 (2019).

[36] S. A. Tawfik, S. Ali, M. Fronzi, M. Kianinia, T. T. Tran, C. Stampfl, I. Aharonovich, M. Toth, and M. J. Ford, *First-principles investigation of quantum emission from hBN defects*, Nanoscale **9**, 13575 (2017).

[37] M. Mackoit-Sinkevičienė, M. Maciaszek, C. G. Van de Walle, and A. Alkauskas, *Carbon dimer defect as a source of the 4.1 eV luminescence in hexagonal boron nitride*, Applied Physics Letters **115**, 212101 (2019).

[38] C. G. Van De Walle and J. Neugebauer, *First-principles calculations for defects and impurities: Applications to III-nitrides*, Journal of Applied Physics **95**, 3851 (2004).

[39] C. Schreyvogel, V. Polyakov, R. Wunderlich, J. Meijer, and C. E. Nebel, *Active charge state control of single NV centres in diamond by in-plane Al-Schottky junctions*, Scientific Reports **5**, 12160 EP (2015), article.

[40] W.-J. Yin, S.-H. Wei, M. M. Al-Jassim, and Y. Yan, *Prediction of the chemical trends of oxygen vacancy levels in binary metal oxides*, Applied Physics Letters **99**, 142109 (2011).

[41] L. A. Ledebo and B. K. Ridley, *On the position of energy levels related to transition-metal impurities in III-V semiconductors*, Journal of Physics C: Solid State Physics **15**, L961 (1982).

[42] M. J. Caldas, A. Fazzio, and A. Zunger, *A universal trend in the binding energies of deep impurities in semiconductors*, Applied Physics Letters **45**, 671 (1984).

[43] P. Dorenbos, *Charge transfer bands in optical materials and related defect level location*, Optical Materials **69**, 8 (2017).

[44] C. G. Van de Walle and J. Neugebauer, *Universal alignment of hydrogen levels in semiconductors, insulators and solutions*, Nature **423**, 626 (2003).

[45] M. Fox, *Optical Properties of Solids* (Oxford University Press, Oxford, 2010).

[46] A. Alkauskas, J. L. Lyons, D. Steiauf, and C. G. Van de Walle, *First-Principles Calculations of Luminescence Spectrum Line Shapes for Defects in Semiconductors: The Example of GaN and ZnO*, Physical Review Letters **109**, 267401 (2012).

[47] M. Lax, *The Franck-Condon Principle and Its Application to Crystals*, The Journal of Chemical Physics **20**, 1752 (1952).

[48] R. Kubo and Y. Toyozawa, *Application of the Method of Generating Function to Radiative and Non-Radiative Transitions of a Trapped Electron in a Crystal*, Progress of Theoretical Physics **13**, 160 (1955).

[49] J. J. Markham, *Interaction of Normal Modes with Electron Traps*, Reviews of Modern Physics **31**, 956 (1959).

[50] A. Alkauskas, B. B. Buckley, D. D. Awschalom, and C. G. V. de Walle, *First-principles theory of the luminescence lineshape for the triplet transition in diamond NV centres*, New Journal of Physics **16**, 073026 (2014).

[51] L. Shi, K. Xu, and L.-W. Wang, *Comparative study of ab initio nonradiative recombination rate calculations under different formalisms*, Physical Review B **91**, 205315 (2015).

[52] A. Baiardi, J. Bloino, and V. Barone, *General time dependent approach to vibronic spectroscopy including franck-condon, herzberg-teller, and duschinsky effects*, Journal of Chemical Theory and Computation **9**, 4097 (2013).

[53] T. Miyakawa and D. L. Dexter, *Phonon Sidebands, Multiphonon Relaxation of Excited States, and Phonon-Assisted Energy Transfer between Ions in Solids*, Physical Review B **1**, 2961 (1970).

[54] D. V. Lang, *Deep level transient spectroscopy: A new method to characterize traps in semiconductors*, Journal of Applied Physics **45**, 3023 (1974).

[55] D. Wickramaratne, C. E. Dreyer, B. Monserrat, J.-X. Shen, J. L. Lyons, A. Alkauskas, and C. G. Van de Walle, *Defect identification based on first-principles calculations for deep level transient spectroscopy*, Applied Physics Letters **113**, 192106 (2018).

[56] C. Hurtes, M. Boulou, A. Mitonneau, and D. Bois, *Deep-level spectroscopy in high-resistivity materials*, Applied Physics Letters **32**, 821 (1978).

[57] P. Hohenberg and W. Kohn, *Inhomogeneous Electron Gas*, Physical Review **136**, B864 (1964).

[58] W. Kohn and L. J. Sham, *Self-Consistent Equations Including Exchange and Correlation Effects*, Physical Review **140**, A1133 (1965).

[59] J. P. Perdew, K. Burke, and M. Ernzerhof, *Generalized Gradient Approximation Made Simple*, Physical Review Letters 77, 3865 (1996).

[60] K. Berland and P. Hyldgaard, *Exchange functional that tests the robustness of the plasmon description of the van der Waals density functional*, Phys. Rev. B **89**, 035412 (2014).

[61] L. Gharaee, P. Erhart, and P. Hyldgaard, *Finite-temperature properties of nonmagnetic transition metals: Comparison of the performance of constraint-based semilocal and nonlocal functionals*, Physical Review B **95**, 085147 (2017).

[62] J. P. Perdew, M. Ernzerhof, and K. Burke, *Rationale for mixing exact exchange with density functional approximations*, The Journal of Chemical Physics **105**, 9982 (1996).

[63] A. Alkauskas, P. Broqvist, and A. Pasquarello, *Defect Energy Levels in Density Functional Calculations: Alignment and Band Gap Problem*, Physical Review Letters **101**, 046405 (2008).

[64] C. Adamo and V. Barone, *Toward reliable density functional methods without adjustable parameters: The PBE0 model*, The Journal of Chemical Physics **110**, 6158 (1999).

[65] J. Heyd, G. E. Scuseria, and M. Ernzerhof, *Hybrid functionals based on a screened Coulomb potential*, The Journal of Chemical Physics **118**, 8207 (2003).

[66] J. Heyd, G. E. Scuseria, and M. Ernzerhof, *Erratum: "Hybrid functionals based on a screened Coulomb potential" [J. Chem. Phys. 118, 8207 (2003)]*, The Journal of Chemical Physics **124**, 219906 (2006).

[67] Y. Jia, S. Poncé, A. Miglio, M. Mikami, and X. Gonze, *Assessment of First-Principles and Semiempirical Methodologies for Absorption and Emission Energies of Ce^{3+}-Doped Luminescent Materials*, Advanced Optical Materials **5**, 1600997 (2017).

[68] S. Lany and A. Zunger, *Assessment of correction methods for the band-gap problem and for finite-size effects in supercell defect calculations: Case studies for ZnO and GaAs*, Physical Review B **78**, 235104 (2008).

[69] H.-P. Komsa, N. Berseneva, A. V. Krasheninnikov, and R. M. Nieminen, *Charged Point Defects in the Flatland: Accurate Formation Energy Calculations in Two-Dimensional Materials*, Physical Review X **4**, 031044 (2014).

[70] H.-P. Komsa, N. Berseneva, A. V. Krasheninnikov, and R. M. Nieminen, *Erratum: Charged Point Defects in the Flatland: Accurate Formation Energy Calculations in Two-Dimensional Materials [Phys. Rev. X 4, 031044 (2014)]*, Physical Review X **8**, 039902 (2018).